Simultaneous laser-induced fluorescence, particle image velocimetry and infrared thermography for the investigation of the flow and heat transfer characteristics of nucleating vapour bubbles

Citation: Voulgaropoulos, V, Aguiar, GM, Markides, CN and Bucci, M. 2022. "Simultaneous laser-induced fluorescence, particle image velocimetry and infrared thermography for the investigation of the flow and heat transfer characteristics of nucleating vapour bubbles." International Journal of Heat and Mass Transfer, 187.

As Published: 10.1016/J.IJHEATMASSTRANSFER.2022.122525

Publisher: Elsevier BV

Persistent URL: https://hdl.handle.net/1721.1/147086

Version: Final published version: final published article, as it appeared in a journal, conference proceedings, or other formally published context

International Journal of Heat and Mass Transfer 187 (2022) 122525

Contents lists available at ScienceDirect

International Journal of Heat and Mass Transfer

journal homepage: www.elsevier.com/locate/hmt

Simultaneous laser-induced fluorescence, particle image velocimetry and infrared thermography for the investigation of the flow and heat transfer characteristics of nucleating vapour bubbles☆

V. Voulgaropoulos[a], G.M. Aguiar[b], C.N. Markides[a,c,*], M. Bucci[b,**]

[a] Clean Energy Processes (CEP) Laboratory, Department of Chemical Engineering, Imperial College London, London, UK
[b] Department of Nuclear Science and Engineering, Massachusetts Institute of Technology, Cambridge MA 02139, USA
[c] Kutateladze Institute of Thermophysics, Novosibirsk, Russian Federation

ARTICLE INFO

Article history:
Received 30 September 2021
Revised 15 December 2021
Accepted 2 January 2022
Available online 18 January 2022

Keywords:
Boiling
Heat transfer
Infrared
IR
Laser-induced fluorescence
Optical diagnostics
PIV
Thermometry

ABSTRACT

Boiling is an effective heat removal process, used for heat exchange and thermal management purposes in many technological applications, from the scale of microelectronic devices to nuclear reactors. However, the physical mechanisms involved in this process are not fully understood yet due to the complexity that arises from the many interacting underlying sub-processes involved in the nucleation, growth and detachment of bubbles that occur during the process. Here, we present an advanced methodology based on combined, synchronized high-speed infrared (IR) thermometry, ratiometric two-colour laser-induced fluorescence (2cLIF) and particle image velocimetry (PIV), along with sample results of an experimental investigation conducted in deionized water, aimed at elucidating the mechanisms involved in the bubble lifecycle. IR thermometry is used to measure the time-dependent 2-D temperature and heat flux distributions over a boiling surface, and 2cLIF is used to measure the time-dependent temperature-field in a vertical plane, in the liquid phase around developing bubbles. Furthermore, PIV is used to measure the velocity fields around the bubbles, in the same plane as 2cLIF. The investigation reveals and allows us to quantify fundamental heat transfer aspects such as the contribution of triple contact line evaporation to the bubble growth process, the dynamics of the near-wall superheated liquid layer, the mixing effect produced by bubble growth and departure, convection effects around the bubble, and quenching heat transfer. Specifically, we observe that, in our experiment, with slowly growing bubbles, the microlayer does not form, and the evaporation at the solid-liquid-vapour contact line contributes to approximately one third of the total heat transferred to the bubble. We also observed that the fluid that rewets the dry spot at the bubble base, as the bubble departs from the boiling surface, comes from the near-wall superheated thermal boundary layer adjacent to the bubble, i.e., it is warmer than the fluid in the bulk. We confirm this finding by modelling this quenching heat transfer phase as a transient conduction process.

1. Introduction

Boiling heat transfer is ubiquitous in engineering applications where large heat transfer rates need to be achieved. The list of applications is diverse and wide-ranging, and includes cooling systems for computer microprocessors and graphical processing units to nuclear reactors and everything in-between. However, while its use is widespread, fundamental questions of this complex phenomenon remain unanswered and the underlying physics are not yet fully understood. The mechanisms involved are highly nonlinear, and micro-scale phenomena such as wetting at the triple liquid-vapour-solid contact line may affect the macroscopic behaviour of the process, determining overall effectiveness. A better understanding of these phenomena and their interplay, which is a crucial requirement in the development of next-generation thermal management systems, can be achieved using advanced computational tools, such as direct numerical simulation (DNS) codes (e.g., see Ref. [1]). These simulations can provide data that are otherwise inaccessible, even with the most sophisticated measurement

Abbreviations: 2cLIF, Two-colour laser induced fluorescence; DNS, Direct numerical simulation; HS, High-speed; IR, Infrared; PIV, Particle image velocimetry; St, Stokes umber.

☆ Revised preprint submitted to International Journal of Heat and Mass Transfer.

* Corresponding author.
** Corresponding author.
E-mail addresses: c.markides@imperial.ac.uk (C.N. Markides), mbucci@mit.edu (M. Bucci).

https://doi.org/10.1016/j.ijheatmasstransfer.2022.122525

Nomenclature

a	Area [m^2]
C	Dye concentration [kg/m^3]
D	Bubble diameter [m]
f	Bubble frequency [1/s]
h	Enthalpy, heat transfer coefficient [J/kg], [W/m^2K]
I	Light flux [W/m^2]
K	Area influence factor [–]
$\mathcal{K}$	Kernel matrix [–]
$\dot{m}$	Mass evaporation rate [kg/s]
N''	Nucleation site density [$1/m^2$]
q''	Heat flux [W/m^2]
R	Ratio of fluorescence intensity, nucleation site density reduction factor [–], [–]
$\mathcal{R}$	Cross-correlation coefficient [–]
s	Temperature sensitivity coefficient [1/ °C]
t	Time [s]
T	Temperature [°C]
u, v	Velocities [m/s]
$\mathcal{W}$	Interrogation window dimension [m]
x, y, $\tilde{x}$, $\tilde{y}$, $\mathcal{X}$, $\mathcal{Y}$, z	Spatial coordinates[m]

Subscripts

0	Incident
a	Absorption
b	Bubble
c	Convective
e	Evaporation
err	Error
F	Fluorescence
FL	Fluorescein
i, j, m, n	Indices
l	Liquid
lv	Liquid-vapour
p	Particle
q	Quenching
r	Relaxation
sat	Saturated
sc	Sliding conduction
SR	Sulforhodamine
v	Vapour
w	Wall, Wait time

Greek symbols

α	Fraction of available light collected [–]
ε	Effusivity, linear extinction coefficient [$Ws^{0.5}/m^2K$], [m/kg]
ζ	Image spatial correlation coefficient [1/m]
λ	Wavelength, swirl [m], [$1/s^2$]
μ	Viscosity [Ns/m^2]
ξ	Image spatial correlation coefficient [1/m]
ρ	Density [kg/m^3]
τ	Characteristic time scale [s]
φ	Fluorescence quantum yield[–]
ω	Vorticity[1/s]

techniques. However, even DNS codes often require sub-grid models, e.g., models of the micro-layer that forms between the vapour bubble and the heated surface as the bubble grows out of its cavity, or the dynamics of the contact angle at the liquid-vapour-solid contact line (e.g., see Ref. [2]) and, furthermore, two-phase DNS tools have a computational cost that is still unaffordable for large-scale applications. Complementary high-resolution experiments are thus also necessary to inform the development of these sub-grid models, but also and importantly, to validate the entire DNS framework, while providing useful data and insight in their own right.

The need for large-scale computational simulations to support the design and safety analysis of engineering systems has fostered the developed of modelling tools that describe the two phases as interpenetrating media and the boiling process with closure relationships (e.g., the boiling heat transfer coefficient) or, more recently, mechanistic models. In fact, most mechanistic models rely on the so-called wall heat flux partitioning approach, which consists of summing the energy removed by the different heat-removal mechanisms expected during the stages of nucleation, growth, and after the departure of bubbles. The simplest heat partitioning scheme for pool boiling consists of three terms, associated with the evaporation of vapour, the quenching of the heated surface when the bubble departs from the surface and the bulk liquid rewets the dry spot formed after the micro-layer has evaporated, and the single-phase natural convection occurring in the regions of the heated surface with no active nucleation sites.

Typical heat partitioning models, e.g., the so-called RPI model [3], comprise three contributions, i.e., evaporation, quenching and single-phase convection, which are evaluated, respectively, as follows:

$$q''_{\mathrm{e}} = fN''\frac{\pi}{6}D_{\mathrm{b}}^3\rho_{\mathrm{v}}h_{\mathrm{lv}} \tag{1}$$

$$q''_{\mathrm{q}} = fN''K\frac{\pi}{4}D_{\mathrm{b}}^2 2\varepsilon_{\mathrm{l}}\sqrt{\frac{t_{\mathrm{w}}}{\pi}}(T_{\mathrm{w}}-T_{\mathrm{l}}) \tag{2}$$

$$q''_{\mathrm{c}} = \left(1-N''K\frac{\pi}{4}D_{\mathrm{b}}^2\right)h_{\mathrm{c}}(T_{\mathrm{w}}-T_{\mathrm{l}}) \tag{3}$$

where N'' is the nucleation site density, f is the bubble departure frequency, D_{b} is the bubble departure diameter, ρ_{v} is the vapour density, h_{lv} is the latent heat of evaporation, ε_{l} is the effusivity of liquid water, t_{w} is the wait time, T_{w} is the wall temperature, h_{c} is the single-phase convection heat transfer coefficient, and T_{l} is the bulk (far-field) temperature of the liquid.

In the relations above, the area influence factor, K, accounts for the fact that when a bubble departs, it carries away the superheated thermal boundary layer from an area larger than $\pi/4\ D_{\mathrm{b}}^2$. Typically $K = 4$, that is, the diameter of the influence area is twice the bubble departure diameter [4]. More recently, Basu et al. [5], Yeoh et al. [6], and Gilman and Baglietto [7] have introduced a fourth term, in order to account for additional heat transfer mechanisms associated with the sliding of bubbles on the boiling surface. In Gilman and Baglietto [7], this sliding bubble term is evaluated as:

$$q''_{\mathrm{sc}} = R_{\mathrm{f}}\ N''f\ a_{\mathrm{sl}}2\varepsilon_{\mathrm{l}}\sqrt{\frac{t_{\mathrm{w}}}{\pi}}(T_{\mathrm{w}}-T_{\mathrm{l}}) \tag{4}$$

where a_{sl} is the area influenced by sliding bubbles and R_{f} is a nucleation site density reduction factor.

The nucleation site density reduction factor used in this expression accounts for the bubbles that coalesce with sliding bubbles as they sweep over other active nucleation sites. Most of the parameters in the heat flux partitioning terms can be measured using infrared thermography [8,9]. However, there are still many open questions related to the characterization of the fluid parameters, e.g., what is the re-wetting temperature T_{l} during quenching heat transfer? Is it the bulk temperature, or it is higher than that? And what are the physical mechanisms that determine the mixing of liquid at the bubble base following the detachment of a bubble from the heated surface and its rise in the fluid?

A few studies in literature have addressed these questions using advanced diagnostics. Non-intrusive rainbow schlieren deflectometry was employed by Narayan et al. [10] to study the liquid

temperature distribution around nucleating and departing single bubbles. When using this technique, collimated light is deflected by thermal gradients present in the liquid, and a colour filter is used to correlate the thermal gradient magnitude to the colour hue, which is captured by a high-speed camera. The formation of the thermal boundary layer and the mixing of the superheated liquid by the departing bubbles could be observed, and the contributions of each heat transfer mechanism was estimated. A drawback of this technique is that the deflection of the light depends on the three-dimensional path of the light rays, thus the measurements are not purely planar. Interferometric measurements were conducted by Yabuki et al. [11] using a He-Ne laser and a Mach-Zehnder interferometer to determine the thermal field around the vapour bubble during its growth and detachment at a spatial resolution of 27 µm/pixel and 4000 frames per second. They could observe the presence of superheated liquid surrounding the bubble and the formation of a warm liquid plume at the trail of the rising bubble, but the spatial resolution was not enough to capture the liquid temperature gradient at the bubble interface. The hydrodynamic interactions between the bubble and the liquid were studied by Takeyama and Kunigi [12] through particle tracking velocimetry of the liquid. They found that the bubble growth and departure pushed and pulled the liquid near the substrate in the horizontal direction, and no vertical mixing of superheater liquid near the heater was generated. A subsequent study by Takeyama et al. [13] placed thermocouple probes at 10 and 100 µm above the surface to observe the liquid temperature variations during nucleate boiling for single and multiple nucleation sites. They observed that the liquid convection created by the bubble interface movement could only peel off the viscous liquid sublayer in contact with the substrate when bubble coalescence occurred close to the boiling surface.

In this work, we discussed the development of an experimental platform that we created to seek an answer to questions related to the heat transfer mechanisms involved in nucleate boiling. This platform involves the use of non-intrusive high-resolution diagnostics. Precisely, we combined infrared (IR) thermometry, two-colour laser induced fluorescence (2cLIF) thermometry, and particle image velocimetry (PIV) to shed light on the dynamics of the bubble growth process. Hereafter, we discuss the principles and the implementation of these techniques, focusing on the 2cLIF thermometry and the PIV, and show samples results related to a single bubble experiment conducted in pool boiling in saturation conditions at atmospheric pressure. As we discuss in the experimental results, we critically analyse the current limitations of this approach, which will be addressed in future developments.

2. Experimental methods

2.1. Boiling cell apparatus

The experimental apparatus and the instrumentation employed for the nucleate boiling experiments are schematically illustrated in Fig. 1. The boiling cell operated at atmospheric pressure and was filled with a solution of deionized (DI) water and the fluorophores used for the two-colours laser-induced fluorescence diagnostics. The cell was brought to its saturation temperature by circulating a warm bath fluid around the boiling cell. The fluid temperature inside the cell was monitored by two K-type thermocouples, one placed adjacently to the heater and the other above it. Four quartz windows symmetrically distributed around the heater laterals provided optical access to the high-speed video (HSV) cameras and the laser sheet. An IR camera was used to measure the temperature distribution on the boiling surface from the bottom of the cell, as shown in Fig. 1.

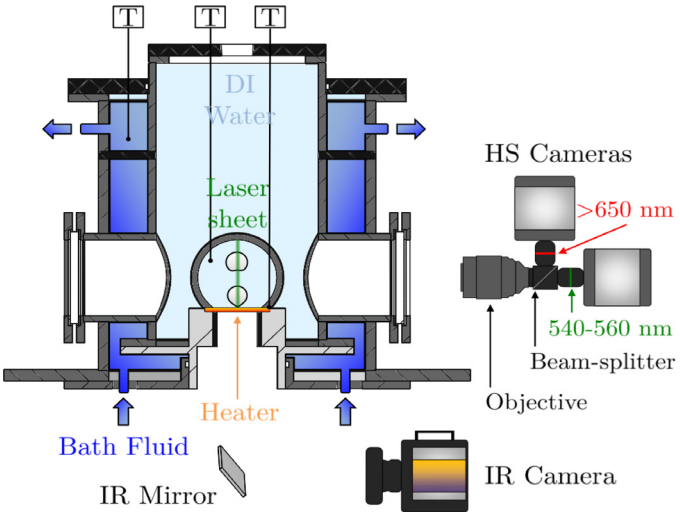

Fig. 1. Schematic illustration of the experimental apparatus and the equipment used for the nucleate boiling experiments.

2.2. Heater

The heater comprises a nano-smooth sapphire substrate coated by a 500 nm thick Titanium film. This titanium film is opaque to light in the 3 to 5 μm wavelength range. It is in contact with water and serves as a Joule-effect heater. Silver pads were deposited on top of the sides of the Titanium coating to provide electrical connections necessary to uniformly energize the heater. The schematic illustration of the heater deposited layers is shown in Fig. 2(a). Sapphire is semi-transparent in the IR range. The thin film titanium coating has negligible thermal capacity and thermal resistance and emits infrared radiation at an intensity that increases monotonically with temperature. This arrangement allows to image precisely the temperature changes induced by the boiling process that occur right at the interface between the wall (i.e., the titanium film) and the liquid. The heating element geometry was designed to generate a 3 $\times$ 3 mm hotspot at its central portion, as indicated in Fig. 2(b). The side voltage taps shown in Fig. 2(b) are used to determine, combined with measurements of the electric current circulating through the heater, the electrical power delivered to the hotspot region. An artificial nucleation site was created at the middle of the hotspot region by etching the sapphire substrate with a focused ion beam. The nucleation site comprises four cavities of 10 μm diameter by 30 μm depth arranged in a square lattice, as shown in Fig. 2(c). The cavities were coated with PTFE polymer to make the artificial nucleation site hydrophobic and facilitate the bubble nucleation.

2.3. Laser-based and infrared imaging equipment

A single cavity of a pulsed high-speed Nd:YLF green laser (527 nm) with 20 mJ per pulse operating at 2.5 kHz was used to excite the fluorophores. Dedicated optics were connected to the laser head to generate a thin sheet of light and to define the measurement volume of the PIV and LIF techniques. The thickness of the laser sheet is 211 µm. This measurement was conducted by using a sharp razor blade connected to a plate with a traversing mechanism and coated with a black dye to avoid any laser reflections. See Appendix A.1 for more details.

Two high-speed (HS) cameras were connected to a pellicle beam splitter (reflectance: 45%; transmittace: 55%) and a Nikon 105 mm lens. An extension tube was connected between each camera and the beam splitter, which also acted as a holder for

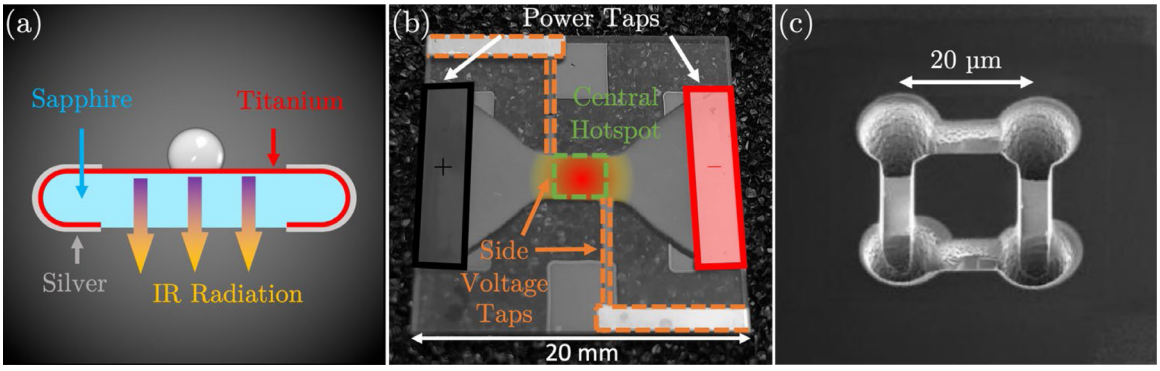

Fig. 2. Heater used in the investigation: (a) schematic illustration of the heater arrangement and materials (not to scale), (b) actual picture of the heater and (c) scanning electron microscope image of the cavities.

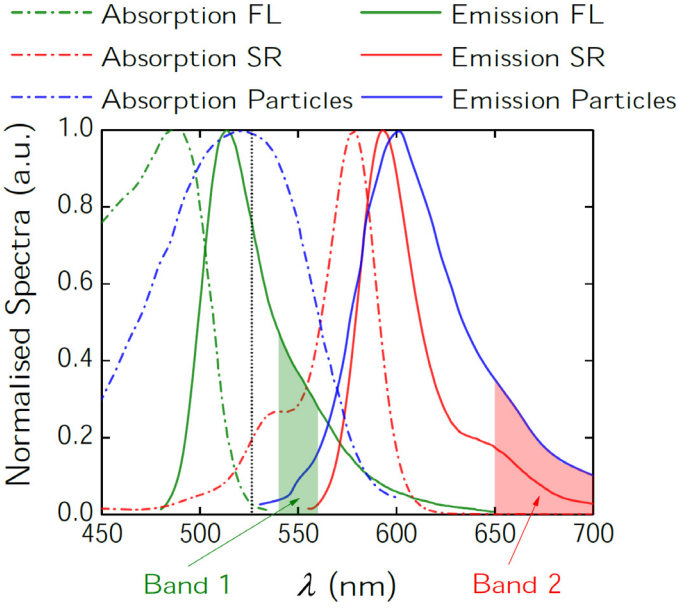

Fig. 3. Absorption (dashed lines) and emission (continuous lines) spectra of the fluorescent dyes and particles employed in the 2cLIF and PTV measurements, respectively, as obtained from the manufacturers. The laser light wavelength is noted with the vertical dotted black line.

the optical filters. Different optical filter arrangements (combinations of short, long and notch filters) were used for each camera to visualize each fluorescent dye separately, as shown in Fig. 3. The first camera, CAM_{FL} (Phantom V12.1), recorded the fluorescent intensity of the temperature-sensitive fluorescent (fluorescein disodium; henceforth denoted as FL) dye (Band 1 in Fig. 3), while the second camera, CAM_{SR} (Phantom V25.12), recorded fluorescence intensity of the temperature-insensitive (sulforhodamine 101; henceforth denoted as SR) dye (Band 2 in Fig. 3). The setup allowed achieving a pixel resolution of 14 µm/pixel and 9.5 µm/pixel with the CAM_{FL} and CAM_{SR} cameras, and a temporal resolution of 0.4 ms. Both cameras have a sensor size of 1280 × 800 pixels with 12 bits per pixel.

A Telops M3k high-speed infrared camera was used to image the boiling surface through the sapphire substrate. The infrared radiation emitted by the heater is reflected by an IR mirror made of gold. The pixel and temporal resolution of the IR camera setup are 31 µm/pixel and 0.4 ms, respectively. The maximum camera sensor size is 320 × 256 pixels with 16 bits per pixel.

A high-speed controller was used to synchronize the triggering signal for the laser light, high-speed video cameras, infrared camera and the heater power generation. The cameras and the laser are synchronized to operate at a frequency of 2.5 kHz. The boiling experiments are run in a transient manner to capture a single isolated bubble and avoid any interaction effects. The camera recordings and the laser pulses are started when the heater is initially off, and the liquid phase is quiescent. The heater is turned on after 200 ms of recording time and its temperature rises to a level where bubble nucleation occurs. It is important to capture the formation of the first bubble because the thermal boundary layer that is formed on top of the heater remains undisrupted. This procedure allows to suppress bubble interaction effects and guarantees that the bubble will be initially surrounded by a superheated liquid layer when it nucleates.

2.4. Techniques

2.4.1. Two-colour laser-induced fluorescence

Laser-induced fluorescence (LIF) can be used to obtain pointwise scalar measurements of temperature in the liquid phase (water). These measurements are achieved via spatiotemporal recordings of the fluorescence of a tracer (specifically an organic dye) that possesses a highly temperature-dependent quantum yield and/or absorption coefficient at the excitation wavelength. A collimated beam of light (at the absorption wavelength λ_a) of uniform depth in the z direction is absorbed when passed through a fluorescent solution, and the absorption for a beam path $\partial x \partial y$ can be described as [14]:

$$\partial^2 I_0(x,y) = -\varepsilon\ C\ I_0(x,y)\partial x \partial y \tag{5}$$

where I_0 (W/m^2) denotes the incident light flux at point (x, y) along the beam path, ε (m/kg) is the linear extinction coefficient of the dye and C (kg/m^3) is the dye concentration, which is assumed uniformly mixed in the fluid.

We work with a pulsed high-energy laser with a laser-pulse duration of the order of a few ns, where the fluorescence is no longer proportional to the excitation intensity ($\neq (I_f \propto I_0)$), most fluorescent molecules in the beam path are excited, and the fluorescence intensity becomes less dependent on the excitation intensity. The fluorescence intensity received by the optics is then given by:

$$\partial^2 I_f = \alpha\ C\ \varphi\ \varepsilon\ \frac{I_0(x,y)}{1 + I_0(x,y)/I_{sat}} \partial x \partial y \tag{6}$$

where α is the fraction of the available light collected, I_{sat} is the saturation intensity of the fluorescent dye, reported typically in

the order of MW/cm^2 [11–13], and φ is the fluorescence quantum yield.

In this work, the liquid temperature measurements need to be performed in the presence of moving vapour-liquid interfaces (growing bubbles), which exhibit strong refractive index gradients, resulting in unpredictable spatial and temporal fluctuations of $I_0(x, y)$ that stem from reflection and refraction of the incident light on the liquid-vapour interface, but also on the liquid-solid surface (reflections of the laser light on the outer layers of the heater). In order to decouple those effects from Eq. (6) and prevent erroneous measurements close to the phase boundaries, a ratiometric two-colour laser-induced fluorescence (2cLIF) method is implemented by employing a pair of fluorescent dyes, namely a dye with a temperature-dependent fluorescence (fluorescein disodium; henceforth denoted as FL) at a mass concentration $C_{FL} = 2.695$ kg/m^3, and a dye with a fluorescence independent of temperature (sulforhodamine 101; henceforth denoted as SR) at a mass concentration $C_{SR} = 0.15$ kg/m^3. Their concentrations are kept constant throughout the experiments, as the water volume in the cell is maintained at the same level between each run, while both FL and SR are heavy molecules and can be assumed not to evaporate.

Each dye is collected separately with a high-speed camera using appropriate optical filters (see Section 2.1.4). Their absorption and emission are shown in Fig. 3 together with the detection band of each camera. FL is selected, because it retains a high temperature sensitivity, even at $I_0 \gg I_{sat}$. The dyes have also been selected in such way to avoid spectral mixing (see Fig. 3). Neglecting those effects, the ratio of the signals $I_{f,SR}$ and $I_{f,FL}$ in the two detection bands 2 and 1, respectively, can be derived from Eq. (6) and according to Chaze et al. [16], as:

$$R = \frac{I_{f,SR}}{I_{f,FL}} \propto \frac{\varepsilon_{SR}}{\varepsilon_{FL}} \frac{C_{SR}}{C_{FL}} \frac{1 + \frac{I_0}{I_{sat,FL}}}{1 + \frac{I_0}{I_{sat,SR}}} \tag{7}$$

where the last term denotes the saturation ratio R_{sat}. As the experiments are performed with $I_0 \approx I_{sat}$ (partially saturated regime), we find from Eq. (7) that the ratio $R(R_0, \varepsilon(T))$ is only dependent on the fluid temperature via the extinction coefficient of FL. Note that the 2cLIF technique is suitable for imaging only half of the portion of the liquid adjacent to each bubble because the laser light is obstructed by the reflections at the liquid/vapour interface. For the same reason, this technique is restricted for imaging a single bubble at a time provided that the light path is not obstructed by bubbles growing adjacently to the region of interest.

2.4.2. Particle image velocimetry

Particle image velocimetry (PIV) is used together with the 2cLIF, to allow us to obtain simultaneously a two-dimensional field of two-component velocity vectors, u and y, along the longitudinal (x) and lateral (y) directions. The displacement of tracer particles between two singly exposed successive images (at time instance t and $t + \Delta t$) is computed by performing space-time cross-correlation in small areas (interrogation windows) with dimensions $\mathcal{W}$. A two-dimensional correlation map is obtained for each window, as:

$$\mathcal{R}(\Delta X) = \int_{\mathcal{W}} I_{f,t}(X) I_{f,t+\Delta t}(X + \Delta X) \mathrm{d}X \tag{8}$$

and the most prominent value of $\mathcal{R}$ in each window dictates the displacement vector $U = \Delta X / \Delta t$ of the tracer particles.

The velocity vector of the particles and the liquid will be identical (allowing us to obtain the velocity of the water) when the particles Stokes number is significantly smaller than unity $St_p = \tau_r/\tau_U \ll 1$, i.e., the relaxation time of the particles is significantly smaller than the characteristic time-scale of the flow field, $\tau_r \ll \tau_U$, where $\tau_r = \rho_p d_p^2 / 18\mu_l$ (ρ_p is the particle density, d_p is the particle mean size, and μ_l is the liquid viscosity), while $\tau_U = \mathcal{O}\{0.1\}$ s is the time scale of the flow induced by the bubble growth. We use polystyrene fluorescent tracer particles ($\rho_p \approx 1000$ kg/m^3, $d_p \approx 10$ μm) with spectral properties shown in Fig. 3 (all properties reported as given by the manufacturer: MicroParticles), resulting in $St_p = \mathcal{O}\{10^{-5}\}$, i.e., any tracing errors can be neglected [17]. Dye leaching of the polystyrene particles is observed due to the elevated temperatures of the water. However, the short duration of the experiment ensures that enough particles are present to perform PIV measurements, despite their initial low concentration (below 0.01 M), which is selected to avoid any interference of the tracers with the nucleation process [18], as demonstrated in Appendix B.3. Particle tracking velocimetry (PTV) measurements could also be considered but is not deemed necessary from the results of the PIV error analysis, which are discussed in Section 4.2.

2.4.3. Infrared thermography

The high-speed infrared camera is used to record the radiation emitted by the opaque thin film titanium heater within the range of 3 – 5 μm wavelength. In this range, the sapphire substrate partially absorbs and re emits the infrared radiation and its absorption coefficient is highly dependent on the infrared light wavelength. Thus, the presence of sapphire contaminates the infrared radiation emitted by the thin titanium film. Additional contamination is caused by the reflection of the background radiation. To overcome this issue, we developed a calibration technique that consist in solving an inverse problem coupling 3-D heat conduction and 2-D optical radiation. For the details of this technique and its implementation, the reader is directed to Ref. [19]. Using this technique, we can reconstruct from the total radiation, the individual emission contributions from the thin film heater, semi-transparent substrate (sapphire) and background reflections. This allows measuring the time-dependent temperature distribution on the boiling surface, as well as the distribution of the heat flux from the solid to the fluid, liquid or vapour.

3. Image analysis, data postprocessing and measurement errors

3.1. Laser-based measurements

3.1.1. Spatial calibration and corrections

To transform the image coordinates $(\tilde{x}, \tilde{y})$ to physical coordinates (x, y), we record images of a calibration plate, with a grid of printed dots of known size and separating distance, using a back light. The calibration plate is fitted on a 3-D printed bespoke holder and is placed in the field of view of the cameras and at the middle plane of the heater surface (i.e., $z \cong 0$). Using these images, and neglecting any geometrical aberrations, the location of each grid point in the image plane coordinates is tracked using the DaVis 10.0 software environment provided by the laser system manufacturer (LaVision). Using the same software, 3rd-order polynomial functions $d\tilde{x}$ and $d\tilde{y}$ with variables $\mathcal{X}$ and $\mathcal{Y}$ are fitted, expressed as:

$$d\tilde{x} = \sum_{i=0}^{3} \sum_{j=0}^{3} \zeta_{ij} \mathcal{X}^i \mathcal{Y}^j \tag{9}$$

$$d\tilde{y} = \sum_{i=0}^{3} \sum_{j=0}^{3} \xi_{ij} \mathcal{X}^i \mathcal{Y}^j \tag{10}$$

where the coefficients ζ and ξ are obtained by the least-square method for each camera. The standard deviations of fit are 2.65 pixels and 2.27 pixels for the SR and FL cameras, respectively.

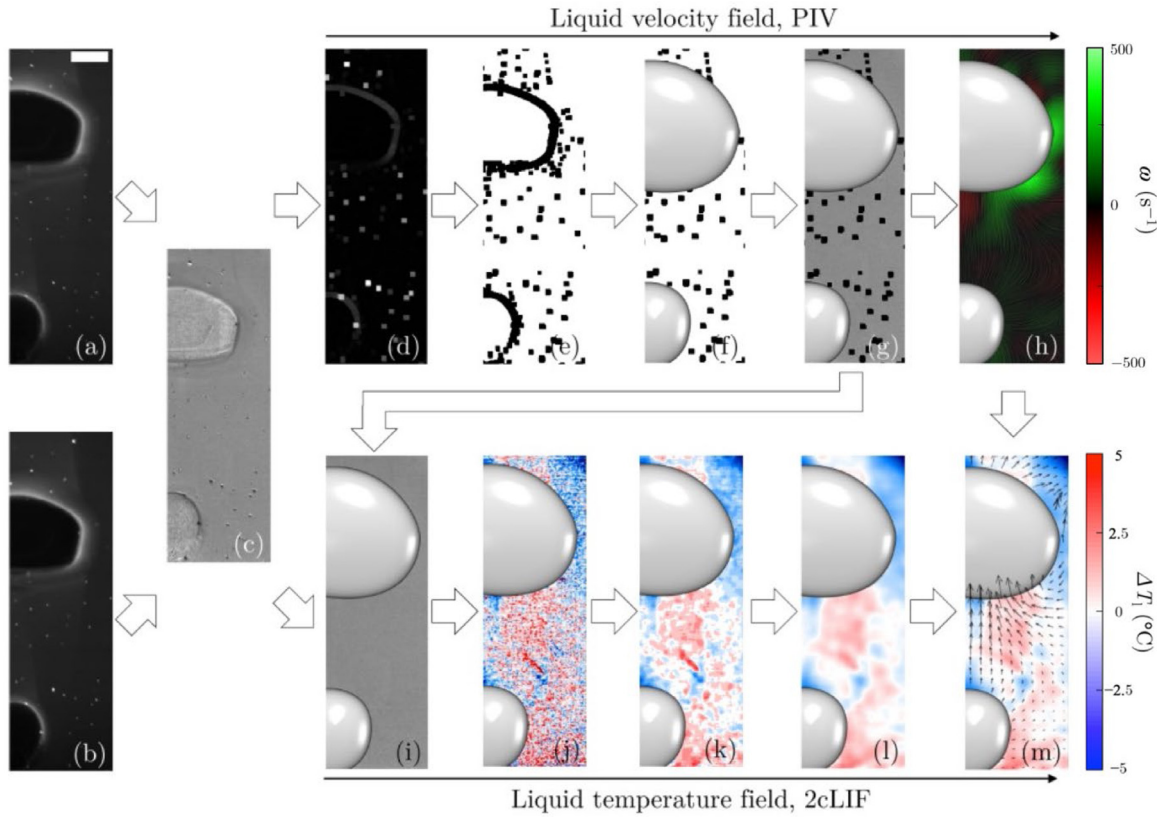

Fig. 4. Image analysis procedure followed for the simultaneous two-colour laser-induced fluorescence (2cLIF) and particle image velocimetry (PIV) measurements: (a) spatially corrected image of SR camera, $I_{f,SR}$; (b) spatially corrected image of FL camera, $I_{f,FL}$; (c) ratio, R, of the spatially corrected images (a) and (b); (d) image (a) subtracted from its own sliding average; (e) non-linear dilatation of (d); (f) filtered particles after masking the bubbles interface; (g) ratio R with masked particles (multiplication of (f) and (c)); (h) PIV velocity field/streamlines; (i) interpolated image of (g); (j) converted temperature field from (i) using the corrected equation of Fig. 5; (k) median filtering in 9 × 9 pixels^2 areas of (j); (l) mean filter over 19 × 19 pixels^2 areas of (k); (m) combined visualization of the liquid velocity and temperature measurements. The scale bar in (a) corresponds to a length of 1 mm.

The final mapping of the coordinates results from:

$$\tilde{x} = x - d\tilde{x}(\mathcal{X}(x), \mathcal{Y}(y)) \tag{11}$$

$$\tilde{y} = y - d\tilde{y}(\mathcal{X}(x), \mathcal{Y}(y)) \tag{12}$$

with $\mathcal{X}(x) = 2(x - 364.7)/1280)$ and $\mathcal{Y}(y) = 2(y - 384.9)/800)$. This procedure compensates automatically for camera misalignment and distortion due to refraction by the interfaces and provides pixel-to-pixel correspondence between the two cameras (which is necessary as the two cameras have a different pixel resolution), which is impertinent to implementing the 2cLIF method (see Eq. (7)). A similar procedure is discussed in detail in Sakakibara and Adrian [20]. The final dewarped images (i.e., for both cameras) have a pixel resolution of 86.0 pixels/mm and a size of 1313 × 883 pixels^2. Figs. 4(a) and (b) illustrate the raw, spatially corrected images of the SR and FL cameras, respectively. Note that the PIV particles are visible on both cameras.

3.1.2. Liquid-vapour phase field

We masque the images manually, following the points of reflections and refractions along the perimeter of the bubble, and smooth the manually drawn areas using a two-dimensional convolution of the masque $\tilde{I}_{mask}(x, y)$ and a kernel matrix $\mathcal{K}(m, n)$ (i.e., a 5 × 5 array, with values equal to 1/25), providing the smoothed masque as:

$$I_{mask}(x, y) = \sum_m \sum_n \mathcal{K}(m, n) \cdot \tilde{I}_{mask}(x - m + 1, y - n + 1) \tag{13}$$

This method is found to provide reliable and pixel-accurate masking of the bubbles. However, for future investigations, we may consider combining these laser techniques with backlit shadowgraphy to obtain the exact location of the liquid-vapour interface with a simple edge detection algorithm.

3.1.3. Liquid velocity field

The images are pre-treated to isolate the particle signal and perform the PIV measurements. The images are filtered with a sliding average of length scale equal to 5 pixels using DaVis 10.0 (LaVision), computing the average at pixel $\boldsymbol{i}$ as:

$$\bar{I}_f(i) = 0.8\bar{I}_f(i - 1) + 0.2I_f(i) \tag{14}$$

The filter is applied four times (along both x and y directions, i.e., left to right, right to left, top to bottom and bottom to top) through the image. The effect is a sliding average, where each new pixel is added with a small weighting factor. The resulting image is then subtracted from the initial image, acting as a high-pass filter, filtering out the local mean background intensity and leaving only the local fluctuations, i.e., the particle signal. The subtracted sliding average image is shown in Fig. 4(d). These images are then used (after being joined with their phase-masked equivalents) for the multi-pass time-resolved cross-correlation (Eq. (8)), which is implemented within DaVis 10.0. The first pass is performed with non-weighted windows $\mathcal{W}$ of 256 × 256 pixels^2 with 50% overlap (interpolated vectors), followed by four passes with non-weighted windows of 128 × 128 pixels^2 with 75% overlap, resulting in a vector spacing of 0.37 mm. Postprocessing is employed only in the

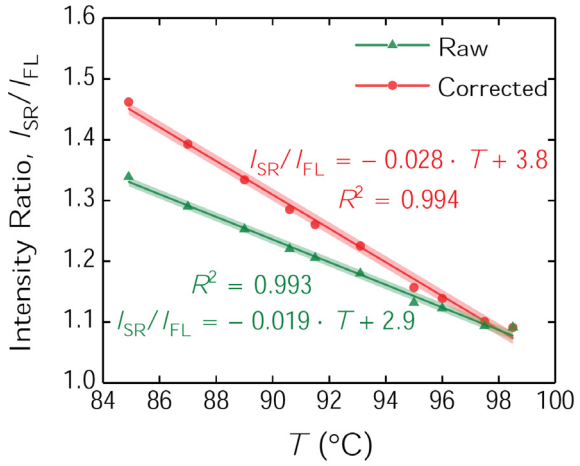

Fig. 5. Calibration curve showing the fluorescence emission intensity ratio, I_{SR}/I_{FL}, as a function of the liquid temperature T, which was measured with a thermocouple of ±0.1 °C accuracy, in a mixed bulk of uniform temperature.

final pass, applying a universal outlier detection over 5 × 5 pixels^2 areas and interpolating all empty correlation windows outside of the masque. This step is particularly important, due to the low particle concentration.

3.1.4. Liquid temperature field

The first step before following the 2cLIF analysis is to remove the tracer particles from the untreated ratiometric image (Fig. 4(c)), which is achieved by applying a non-linear dilatation filter to the image of Fig. 4(d) (implemented via DaVis 10.0) over 7° × 7° pixels^2 areas, sorting all elements according to their intensity. The elements are stored back in their respective area, storing the next after the middle element as the new central pixel (Fig. 4(e)). This non-linear operation tends to change the mean image intensity and therefore this image should not be used within the intensity-based 2cLIF algorithm, but merely for masking the particle signal out of the images by thresholding.

The images are then passed on to MATLAB (MathWorks). The non-particle pixels are filled with the values of the initial ratiometric image, while the particle pixels are replaced by NaN values (Fig. 4(g)). Then, the NaN values are interpolated using the Laplacian equation in the equally spaced grid, as:

$$\frac{\partial^2 I_f}{\partial x^2} + \frac{\partial^2 I_f}{\partial y^2} = 0 \tag{15}$$

This partial differential equation is solved for any node in the grid with finite differences, replacing the NaN pixel values by the average of its four neighbours. The resulting image, Fig. 4(i), is identical (same intensity) as the initial ratiometric one (Fig. 4(c)), but with the NaN pixels (from the particle signal) interpolated.

The untreated temperature field of Fig. 4(j) is then achieved by performing a spatially resolved calibration over 30 × 30 pixels^2 windows (to minimize random errors), eventually transforming pixel counts to absolute temperatures. The spatially resolved calibration curve is obtained at the end of the experimental runs, by cooling down the liquid uniformly (isothermal condition ensured with the presence of the two thermocouples and a mixer) and recording 500 images at various reference temperatures, spanning a range of about 15 °C. It has been shown that the relationship between the temperature and the ratio of SR and FL can be described accurately by a linear fitting [11,13], as it is shown for our work in Fig. 5 for a typical window. The coefficients of determination are found above 0.98 throughout the whole region of interest, giving confidence in the linear fitting used. The ratio of the fluorescence signal variation at T and T_0 can be described as:

$$\frac{I_{f,T}}{I_{f,T_0}} = \exp[s \cdot (T - T_0)] \tag{16}$$

where s is a coefficient describing the temperature sensitivity and is equal to: $s = 1/I_f \cdot dI_f/dT$ or ~1.9%/°C (slope of the curve), which is lower than the previously reported values for these dyes [9,11].

It has been found that sulforhodamine 101 (or its 640 equivalent) degrades at elevated temperatures [15]. We, therefore, kept the overall duration of the experiment, including the measurement and calibration runs, below 60 min to prevent such effects. Nevertheless, it is found that degradation is impairing I_{SR} early on and for this reason, we correct for the thermal degradation effects depending on the acquisition time of each run (see more details in Appendix B.1). The corrected curve is also shown in Fig. 5 for the same typical case and location. The corrected calibration curve exhibits sensitivity values of about 2.8%/ °C, which is very close to the reported literature values. Photodegradation effects are not considered. Both dyes are found to photodegrade, but at substantially higher pulse numbers than those used throughout the whole experiment (see more details in Appendix B.2). Finally, the temperature field is smoothed using a median and a mean filter (Figs. 4(j)-(l)).

3.2. Infrared thermography

Processing of the images collected by the infrared camera is performed using the calibration algorithm introduced in Section 2.4.3 and discussed in detail in Ref. [19]. The calibration algorithm allows for measurements of the time-dependent temperature and heat flux distributions over the boiling surface. The triple contact line at the bubble base was tracked by simply using an adaptive threshold binarization of the heat flux maps. This is possible because, at the solid-liquid-vapour contact line, the heat flux from the solid to the fluid is significantly higher than the average heat flux, as discussed in the results section of this paper. Also, the heat flux at the dry spot formed underneath the bubble is significantly lower than the heater regions occupied by the liquid phase and the solid-liquid-vapour contact line. Thus, the infrared thermography measurements exhibit three distinct regions according to the heat flux intensity (e.g., see Fig. 9) that can be easily identified using a simple image thresholding. The spatial accuracy of the image segmentation procedure was later verified visually by checking the superposition of the segmentation with the heat flux distribution.

3.3. Data reduction and measurement errors

The bubble size is quantified by the equivalent bubble diameter (i.e., the diameter of a spherical bubble with the same volume). The bubble volume is estimated through the bubble masque, by assuming a symmetry of revolution. We estimate that this approach has an uncertainty between 2 and 10%, encountered during the final (larger size) and initial (smaller size) times of the bubble growth, respectively. These uncertainties are calculated by measuring the standard deviation of the bubble size obtained through the manual edge detections over 20 trials of the same time-instance. This uncertainty could be reduced by the used of backlit shadowgraphy, which will be implemented in future investigations.

The K-type thermocouples used to measure the water temperature have *a* ±0.1 °C uncertainty, provided by the manufacturer (Omega) for this range of conditions, with a time-response of order $\mathcal{O}\{1\}$ s, which is of same order as the time-scales required to monitor, i.e., ensuring temperature homogeneity between the heater surface and the top of the field of view of the high-speed cameras during the measurement and calibration runs.

It was not possible to derive the error propagation formulas of the 2cLIF method for instantaneous temperature measurements, due to the plethora of parameters that affect it, e.g., alignment of equipment, laser-sheet thickness, pulse to pulse variation, dye types, dye concentrations, thermal and photo-degradation effects, spectral mixing, calibration procedure, image analysis and filtering. Nevertheless, a diligent approach to optimize the aforementioned parameters was followed, in order to minimize 2cLIF measurement errors. We estimate a ±1 °C absolute uncertainty in the liquid temperature (T_l) for the instantaneous measurements in the range of conditions of interest. Sakakibara and Adrian [20] and Shafii et al. [21] reported uncertainty values of ±1.5 °C and ±0.8 °C for instantaneous 2cLIF temperature fields, respectively, albeit different dye-pairs employed, which resulted in approximately half the sensitivity compared to the 2.8%/ °C achieved in our work. More recent works report uncertainties below ±1 °C when using the same dye-pair (which results in a similar measurement sensitivity) as our work [11,13].

We use DaVis 10.0 to quantify the instantaneous velocity uncertainties of the PIV measurements, using the method by Sciacchitano et al. [22]. Fig. 6 illustrates the velocity (Fig. 6(a)) and its gradients (vorticity and swirl, Figs. 6(b) and (c)), as well as their associated errors for a typical time-instance of the nucleation of a second bubble during the transient run at a nominal heat flux of 125 kW/m^2. During the nucleation and departure of the bubble, the errors of both velocity components (Figs. 6(f), (g)) and velocity magnitude (Fig. 6(e)) do not exceed 20%. As shown in Fig. 6(e) and (g), the errors are higher in the vertical velocity component at the top part of the departing bubble, which are also accompanied by low correlation values (< 0.5) (Fig. 6(d)).

The uncertainty in the local temperature measurement on the boiling surface is estimated to be approximately 0.5 °C, and it is practically determined by the uncertainty of the thermocouples used for the calibration of the infrared camera. Instead, the uncertainty on the local heat flux, obtained through the solution of the inverse conduction-optical radiation problem is estimated to be about 10% of the average value for the experimental measurements presented in this paper.

4. Results and discussion

Fig. 7 depicts the bubble equivalent diameter and the bubble base diameter for a test with a heat flux of q" = 125 kW/m^2, extracted from the high-speed video and infrared images, respectively. Under this condition, the first bubble appears 285 ms after the heater power is turned on. The bubble nucleates at a wall superheat ΔT_w of 4.2 K (due to the presence of the engineered hydrophobic site of nucleation) and has a total growth time of 149.6 ms and a departure diameter of 3.06 mm. According to the model of Mikic, Rohsenow and Griffith [23], the transition between the inertia-controlled and the thermally-controlled growth for a bubble nucleating at ΔT_w of 4.2 K occurs approximately at 15 μs. Thus, for the conditions of this study, the bubble growth should occur almost entirely in the thermal diffusion limited regime, i.e., the bubble growth rate is determined by the heat diffusion in the superheated liquid. The growth in the thermal diffusion limited regime is also confirmed by the large differences between the equivalent and the base diameters (see Fig. 7). After about 10 ms, the bubble base diameter remains fairly constant and does not follow the growth of the equivalent diameter. We also found a fairly good agreement between the theoretical growth rate (in the thermal diffusion limited regime) predicted by the model of Mikic et al. [23] and the experimental results, as the predicted and measured bubble equivalent diameters are $D(t) = 10.03\sqrt{t}$ and $D(t) = 8.93\sqrt{t}$ (where D is in mm and t is in s), respectively.

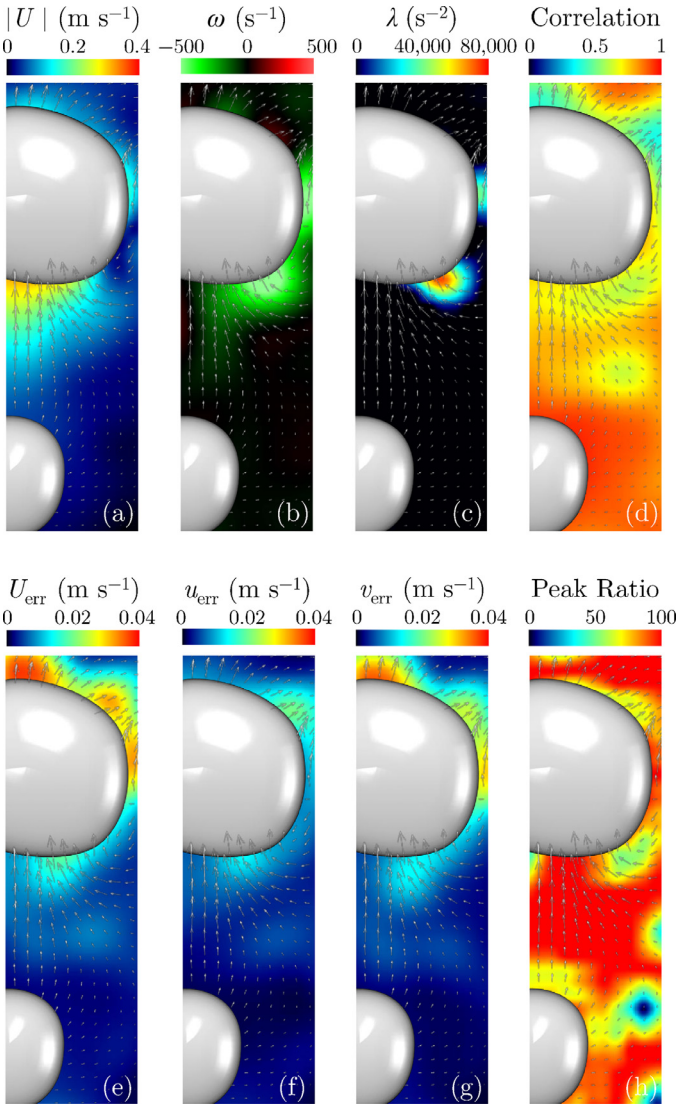

Fig. 6. Uncertainties and correlation characteristics of the two-dimensional two-component particle image velocimetry (PIV) measurements shown for a typical time-instance during the nucleation of a vapour bubble at 125 kW/m^2.

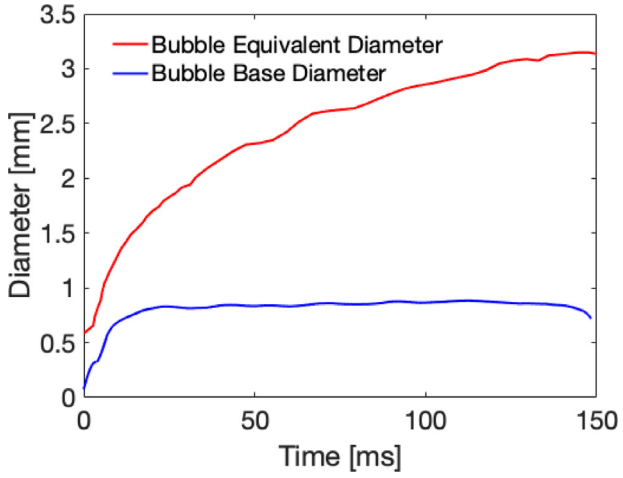

Fig. 7. Bubble equivalent and base diameter during the growth of a vapour bubble at 125 kW/m^2.

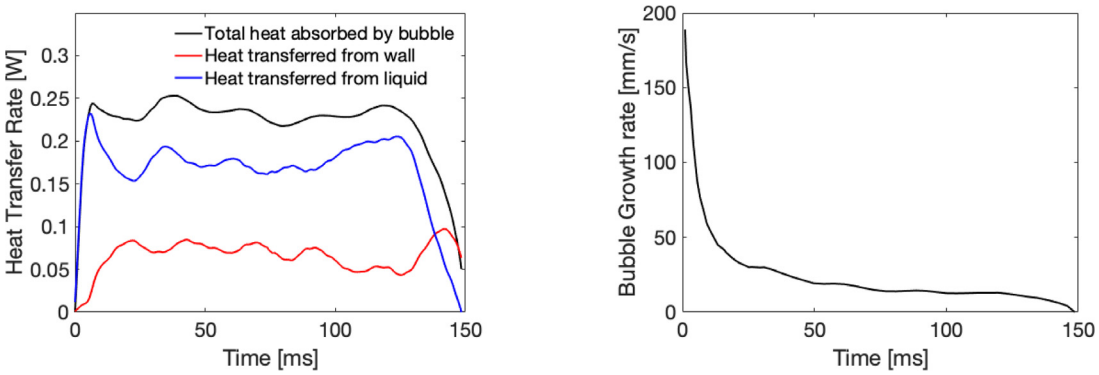

Fig. 8. Bubble heat transfer rates (left) and expansion rate (rate) for a bubble growing with a heat flux input of 125 kW/m^2.

4.1. Energy removed by the bubble

The rate of energy transferred to the bubble is proportional to its growth rate and it can be expressed as:

$$\dot{Q}_b(t) = \dot{m}\ h_{lv} = \left(\rho_v \frac{\pi D(t)^2}{2} \frac{dD(t)}{dt}\right) h_{lv} \tag{17}$$

where ρ_v is the water vapour density at saturation temperature and h_{lv} is the latent heat of evaporation. The heat transferred from the wall to the bubble is estimated from the infrared diagnostics by integrating the heat flux maps underneath the bubble footprint (i.e., within the area defined by the liquid-vapour-solid contact line) in space and time. Ideally, the heat transferred from the liquid to the bubble at the liquid-vapour interface (i.e., far from the wall) could be calculated from the 2cLIF temperature gradients using Fourier's law. However, the relatively low spatial resolution that we could achieve (compared to the thickness of the thermal boundary layer in the liquid) make this estimate currently impossible. Still, the contribution from the liquid heat transfer to bubble was estimated as the difference between the total heat absorbed by the bubble (evaluated through Eq. (17) and the measured equivalent diameter) and the heat removed from the wall (measured with the infrared thermometry technique). The comparison between the net heat absorbed by the bubble and the heat transferred to the bubble from the wall and the liquid vs. time is shown in Fig. 8 (left), whereas the bubble expansion rate is shown in Fig. 8 (right).

From Fig. 8 (left), we verified that the bubble heat transfer rate quickly increases to 0.25 W after 24 ms of the nucleation and then plateaus until the bubble departure. At the initial stages of growth, the heat transferred at the wall (e.g., due to the evaporation at the liquid-vapour-solid contact line) is quite low, and the growth of the bubble is driven by the evaporation of the superheated liquid that surrounds the liquid-vapour interface. As the bubble base grows, the length of the triple contact line increases and the contribution of the wall heat transfer increases until, at approximately 24 ms, the bubble base stops growing. At this point, the value of the heat transferred from the wall starts to oscillate. These oscillations seem to be cause by radial oscillations of the bubble base (and consequently of the length of the solid-liquid-vapour contact line). This behaviour is typical in bubbles growing at a low growth rate, such as the one discussed here (see Fig. 8, right).

The stabilization of the total heat absorbed by the bubble occurring at approximately 24 ms coincides with the stabilization of the bubble base diameter (see Fig. 7) and the plateau of the expansion rate before its departure. The results from Fig. 8 reveal that the evaporation of the triple contact line contributes on average to 32% of the total heat absorbed by the bubble. Furthermore, the total heat removed by the bubble can be obtained from:

$$Q_b = \int_0^{t_g} \dot{Q}_b(t)dt \tag{18}$$

The results indicate that the bubble removed 32.6 mJ of heat at an average rate of 0.22 W. Considering that the average bubble base diameter is 0.81 mm, the average heat flux removed by the bubble from the surface is estimated as 416 kW/m^2, or approximately 3.3 times greater than the applied heat flux.

4.2. Liquid/wall temperature fields and liquid velocity field over the bubble lifecycle

The various stages of the bubble lifetime, starting from its inception, throughout the bubble growth until its detachment from the heated surface were captured simultaneously with the 2cLIF, IR and PIV techniques. An example of these synchronized measurements is shown in Fig. 9 at time instants, where the bubble detachment occurs at t = 149.6 ms (Fig. 9(d)).

Using the ratiometric 2cLIF method we obtained the temperature fields in the bulk and close to the bubble interface. Relatively small temperature gradients were recorded in the bulk and away from the bubble. Note also the passage of a cold liquid plume of liquid (at approximately 95 °C) far away from the heater on the top of Fig. 9 for t larger than 69.2 ms.

At the early stages of the bubble life (Fig. 9(a)), the bubble growth rate is relatively high, and the rapid expansion of the bubble interface pushes the surrounding liquid radially outward. The liquid temperature field in Fig. 9(a) reveal the presence of a superheated liquid layer at approximately 102 °C close to the nucleation site region and the PIV results indicate that the liquid velocity near the vapour-liquid interface is approximately 0.3 m/s, which is in good agreement with the initial bubble expansion velocities obtained through the growth rate of the bubble equivalent diameter reported in Fig. 8(b). At t = 4 ms (Fig. 9(b)) the bubble growth rate has dropped considerably to 0.1 m/s and the velocity fields show that the liquid is still being pushed away from the nucleation site, but at lower velocity, in the order of 0.05 m/s. As the bubble enters its slow growth stage (Fig. 9(c)), we observed that the velocity fields surrounding the bubble are very small, even though the centre of mass of the bubble has risen under the effect of buoyancy forces.

The initial bubble base expansion rate estimated using the infrared diagnostics is in the order of 0.01 m/s (Fig. 7). In such conditions, the bubble base does not expand fast enough to form a liquid microlayer between the vapour phase and the solid surface [24]. The infrared camera results shown in Fig. 9 (top) confirm the absence of the microlayer and reveal that the evaporation of the

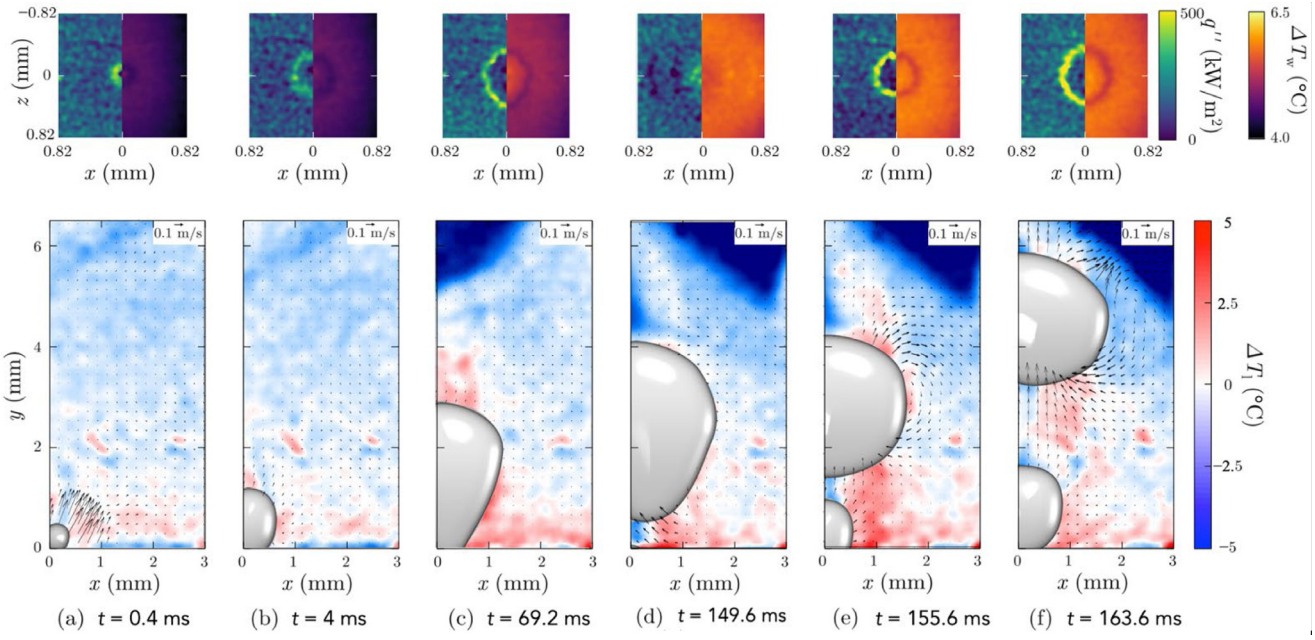

Fig. 9. Measurements performed simultaneously with the 2cLIF, IR and PIV techniques for a bubble growing with a heat flux input of 125 kW/m^2. The top row shows heat flux (left) and temperature (right) maps obtained through the infrared diagnostics. The bottom row shows combined results for the temperature and velocity fields of the liquid obtained through 2cLIF and PIV diagnostics, respectively.

triple-contact line is the main wall heat transfer mechanism during the growth of the bubble. The heat flux at the triple contact line is 3 to 5 times higher than the heater average and its magnitude is in agreement with the findings reported in Ref. [25]. One should also note the temperature at the contact line is much lower than elsewhere. This is the results of a conjugated heat transferred process, as the evaporation of the contact line not only consumes the energy released by Joule heating, but also the sensible heat stored in the sapphire substrate. Note that the bubble base inner region is dry, i.e., the solid surface is in contact with vapour. This vapour has poor heat transfer properties compared to liquid or the evaporation of the triple contact line (i.e., the heat flux in the dry spot is practically negligible). Consequently, the temperature of this dry spot increases, as confirmed by the infrared results in Fig. 9, showing that the centre of the bubble is much warmer than the region adjacent to the bubble covered by the liquid.

In Fig. 9(c) we see that a significant portion of the bubble interface is surrounded by warmer superheated liquid when compared to Fig. 9(a) and (b). The increase of the wall superheat in this region coincides with the decrease of the bubble base diameter growth rate. As the bubble base stops growing, the liquid in this region stagnates and warms up. This superheated liquid may contribute to the growth of the bubble by evaporating at the liquid vapour interface in the vicinity of the wall. However, this mechanism should not be confused with the contact line evaporation. In fact, the heat transfer calculations shown in Fig. 8(a) reveal that for this time instant, the bubble growth is 64% driven by the heat transfer from the superheated liquid and 36% at the wall (i.e., at the contact line).

As the bubble departs from the heated surface and start to rise in the liquid pool (Figs. 9(d) to (f)), the liquid from the bubble top flows towards the bottom of the bubble. However, the velocity of the liquid phase near the heated surface does not seem to be affected by this swirl. What determines the movement of the liquid in the near wall region is rather the contraction of the bubble base (as the bubble departure process begins) and eventually the detachment of the bubble itself. As the bubble base recedes (see Figs. 9(c) and (d)), the centripetal motion of the contact line makes the surrounding liquid to accelerate inward. Then, as the bubble detaches from the surface, its shape changes due to surface tension forces, which tend to make the bubble more spherical. This phenomenon pulls the underneath liquid upward (see Fig. 9(d)). Note that the velocity under the bubble is significantly higher than the velocity at the top of the bubble. This phenomenon pulls the near-wall hot liquid (surrounding the bubble during its growth) towards the nucleation site and mixes the liquid to an extent which is far stronger than the one possibly induced by the natural convection created by density (i.e., temperature) gradients.

As the surrounding liquid rewets the dry spot at the bubble base, a significant amount of energy is transferred from the wall to the liquid by transient conduction. This heat transfer process is often referred to as quenching and constitutes an important heat transfer mechanism. The infrared measurements allow to quantify the local quenching wall heat flux q''_q and the corresponding wall temperature T_w, while the quenching temperature of the liquid T_l can be obtained from the 2cLIF results. Note that this quenching heat flux can be theoretically estimated from [26]:

$$q''_q(t) = \frac{[T_w - T_l]}{\varepsilon_w + \varepsilon_l} \frac{1}{\sqrt{\pi t}} \tag{19}$$

where ε_w and ε_l are the effusivities of the wall (i.e., sapphire) and the liquid (i.e., water), respectively. Fig. 10 shows a comparison between the measured quenching heat flux and the heat flux that can be predicted using Eq. (19). In this figure, $t = 0$ ms coincides with the bubble departure from the surface. Precisely, theoretical predictions using two different modelling approaches are shown. The first approach (solid blue line) consists of using the experimental values for both the wall and the liquid temperatures, which are practically constant at 105.9 °C and 102.5 °C for the 2 ms following the departure of the bubble, before the nucleation of a new one. The second approach (dashed blue line) also considers the measured wall temperature but assumes that the quenching liquid is at bulk temperature, i.e., 100°C. As shown in the figure, the best agreement between the measured heat flux and the two heat fluxes predicted by Eq. (19) is achieved when we use the measured liquid quenching temperature, rather than saturation temperature

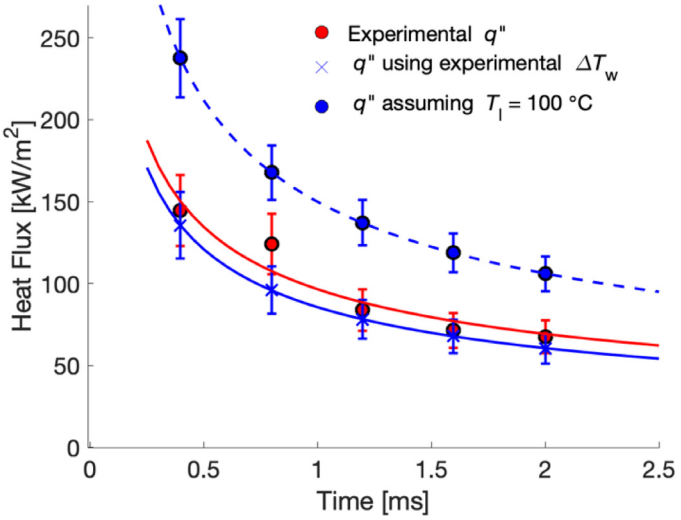

Fig. 10. Quenching wall heat flux promptly after the bubble departure at $q'' = 125$ kW/m^2. Solid curves represent trend lines.

(which leads to an overestimation of the heat flux). This observation is critical, as it undermines the general validity of the assumption often made in heat flux partitioning models, i.e., that the liquid quenching temperature is the bulk temperature. Our results, and the results of Tanaka et al. [27], indicate that the rewetting effective ΔT is in a range between 40 and 55% of the difference between the bulk temperature and the wall temperature. However, more comprehensive studies considering different surfaces and fluids are necessary to understand better how this quantity is affected by flow and bubble dynamics.

5. Conclusions

We combined high-speed infrared thermometry and laser-based diagnostics to obtain a comprehensive picture of the nucleation, growth and departure of vapour bubbles from a heated surface in saturated pool boiling conditions. The nucleation of a bubble was controlled through an artificial cavity coated with a hydrophobic material. The use of these techniques has allowed interesting observations. When bubbles nucleate at low superheat (4 K):

- the slow growth rate avoids the formation of liquid microlayers;
- the energy transfer via evaporation at the liquid-vapour-solid contact line contributes to approximately one third the bubble growth process, while the other portion is transferred through the evaporation of the superheated layer surrounding the bubble;
- the detachment of the bubble promotes liquid mixing near the wall, and the temperature at which the liquid rewets a nucleation site can be higher than the bulk temperature (i.e., saturation temperature in our experiments). This observation has important implications, as is undermines, at least for pool boiling conditions, the general validity of a common modelling assumption made in mechanistic heat flux portioning models, i.e., that the liquid quenches the nucleation site at the bulk temperature.

Generally, the results show the intrinsic coupled nature of the flow and thermal fields, and demonstrate that the combination of such high-resolution and detailed diagnostics can advance our fundamental understanding of the heat and mass transfer mechanisms during nucleate boiling and close the level-of-detail gap between advanced numerical simulations and experiments by providing highly space- and time-resolved benchmark data for the development and validation of accurate and reliable computational tools for the prediction of these phenomena.

Finally, we also identified technical limitations to overcome in the future. For instance, it was impossible to measure temperature gradients in the liquid near the liquid-vapour interface. To achieve this goal, we may need to push the spatial resolution of the 2cLIF technique and to increase its signal to noise ratio. Also, the implementation of backlit shadowgraphy in parallel with the 2cLIF image acquisition can improve the liquid-vapour interface detection. Future efforts will focus on the solution of these issues, and ideally on integrating an additional technique to track the dry spot and possibly the liquid microlayer thickness and extension [28]. Future studies will also address faster growing bubbles nucleating at a much higher wall superheat.

Declaration of Competing Interest

The authors declare that they have no known competing financial interests or personal relationships that could have appeared to influence the work reported in this paper.

CRediT authorship contribution statement

V. Voulgaropoulos: Methodology, Investigation, Software, Validation, Formal analysis, Writing – review & editing, Visualization. **G.M. Aguiar:** Methodology, Investigation, Software, Validation, Formal analysis, Writing – review & editing, Visualization. **C.N. Markides:** Conceptualization, Methodology, Resources, Writing – review & editing, Visualization, Supervision, Project administration, Funding acquisition. **M. Bucci:** Conceptualization, Methodology, Resources, Writing – review & editing, Visualization, Supervision, Project administration, Funding acquisition.

Acknowledgments

This work was supported by the MIT International Science and Technology Initiatives (MISTI) Global Seed Funds, and the Department for International Development (DFID) through the Royal Society-DFID Africa Capacity Building Initiative. VV is grateful to the Imperial College London Dame Julia Higgins Postdoc Collaboration Fund. MB acknowledges funding support from the US Nuclear Regulatory Commission (NRC). The work was also supported by Russian Government "Megagrant" project 075-15-2019-1888. The authors thank Mr. Dimitri Zogg for his input to the experimental measurements and Mr. Chi Wang for his help with the fabrication of the single bubble heater. Data supporting this publication can be obtained on request from cep-lab@imperial.ac.uk or redlab@mit.edu.

Appendix A. Laser characterization

Appendix A.1. Sheet thickness

The laser sheet-thickness was measured with a sharp razor blade fitted to a plate with a traversing mechanism and coated with a black dye to reduce laser reflections. The blade was initially positioned to completely block the laser sheet, resulting in quasi-zero values of fluorescence intensity measured from the cameras. As the blade was gradually moving along the transverse direction and perpendicularly to the laser sheet, the signal recorded by both cameras gradually increased, reaching its maximum value at the position where the blade was no longer blocking the laser sheet. The fluorescence intensity was both space-and time-averaged over an area of $30 \times 30^{\circ}$ pixels^2 and 300 images, respectively. The cumulative distribution of the light intensity is shown in Fig. 11 (left).

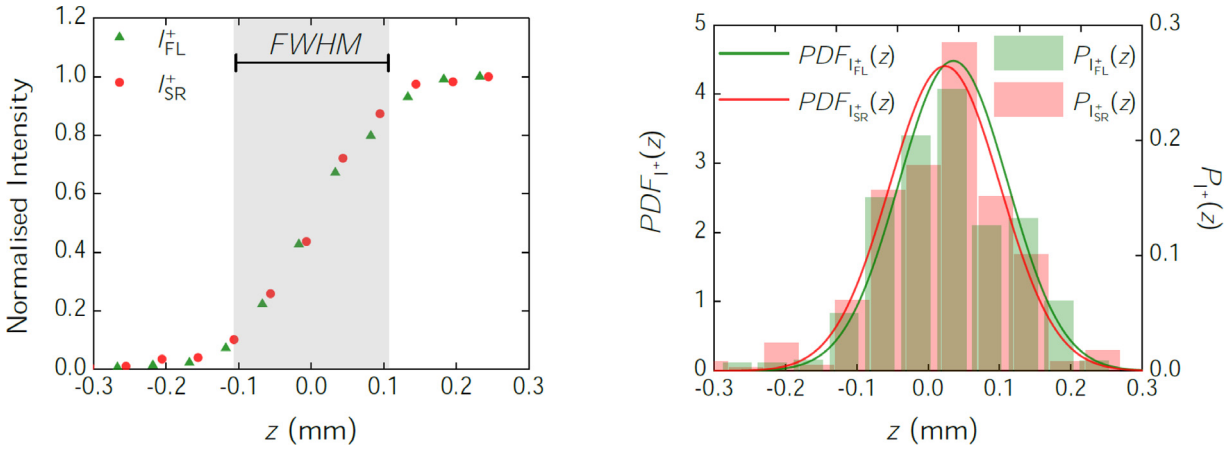

Fig. 11. The laser sheet thickness measured from the fluorescence light recorded from the high-speed cameras as the blade traversed along the transverse direction z: cumulative distribution (left) and probability density function (right).

The respective probability histograms, $P_{I^+}(z)$, are calculated from the spatial gradient of the normalized intensity of each camera $\partial I^+/\partial z$, and each can be described by a Gaussian probability density function $\mathrm{PDF}_{I^+}(z)$ of the form:

$$\mathrm{PDF}_{I^+}(z) = \frac{1}{\sigma\sqrt{2\pi}}\exp\left[-\frac{(z-\mu_z)^2}{2\sigma^2}\right] \tag{20}$$

In the aforementioned relation, the standard deviation is noted as σ and the mean as μ_z. The resulting histograms and PDFs are shown in Fig. 11 (right). The laser sheet-thickness is reported here as the full width half maximum (FWHM) value of the light distribution. The FWHM can be calculated from:

$$\mathrm{FWHM} = 2\sigma\,(2\ln 2)^{0.5} \tag{21}$$

which can be written as $FWHM \approx 2.355\sigma$, corresponding to 209 μm and 213 μm for the fluorescence of I_{SR} and I_{FL}, respectively. The resulting laser sheet-thickness is taken as the mean between the two cameras equal to 211° μm.

Appendix A.2. Pulse to pulse intensity variation

To quantify the variation in the fluorescence emission of the dyes due to pulse-to-pulse energy fluctuation of the laser-sheet, we recorded the fluorescence emission intensity of both dyes (and their ratio) during 500 pulses, while the water in the pool boiling cell was at ambient temperature and continuously stirred to avoid any thermal and photodegradation effects. Fig. 12 shows the modulation of the fluorescence emission intensity of the dyes and their ratio, which are spatially averaged over an area of 30 × 30 pixels^2 and normalized with their respective mean fluorescence emission intensity value over the 500 pulses. The emission from SR varies about the mean by approximately ±3%, the one of FL by ±7% and of their ratio by less than ±1% (probably associated with random noise in the CCD arrays). Light-sheet energy corrections are thus not deemed necessary, as the 2cLIF approach compensates for the fluctuations in the incident illumination intensity between successive laser pulses.

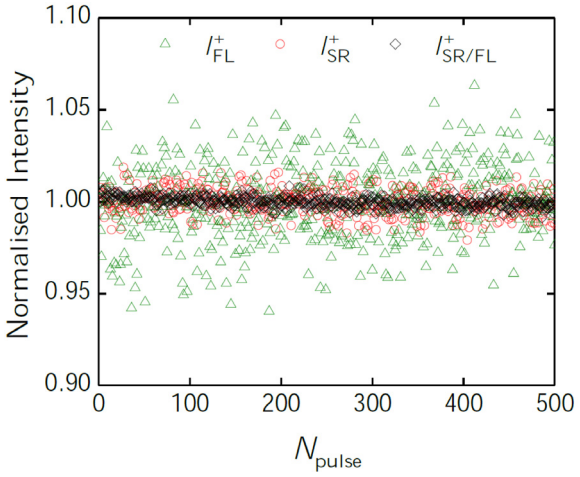

Fig. 12. Variation of the fluorescence intensity of FL, SR (normalized with their corresponding time-averaged value) and their ratio as a function of the number of laser pulses. The liquid in the pool boiling vessel is continuously stirred during these measurements to avoid photodegradation effects.

Appendix B. Fluorescent dyes characterization

Appendix B.1. Thermal degradation effects

It has been found that sulforhodamine 101 (SR) can be subject to thermal degradation when its temperature exceeds the ambient [16]. In our current work, we induced boiling at water saturated conditions ~ 100°C, which resulted in the degradation of SR

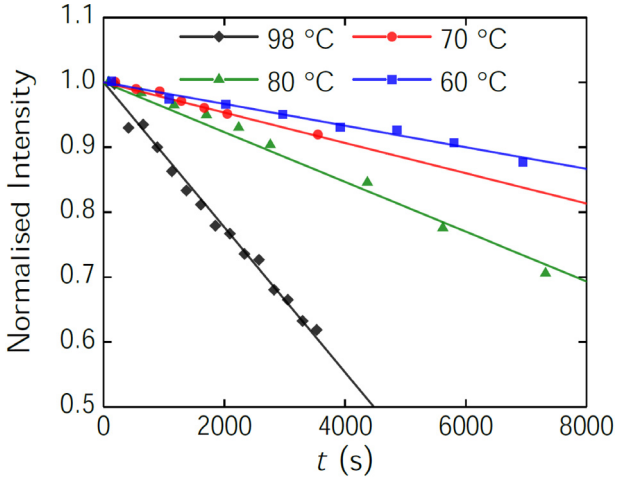

Fig. 13. Thermal degradation for SR at multiple temperatures induced by the elevated solution temperatures. The data for 60–80 °C have been extracted from Chaze et al. [16] and are shown for completeness.

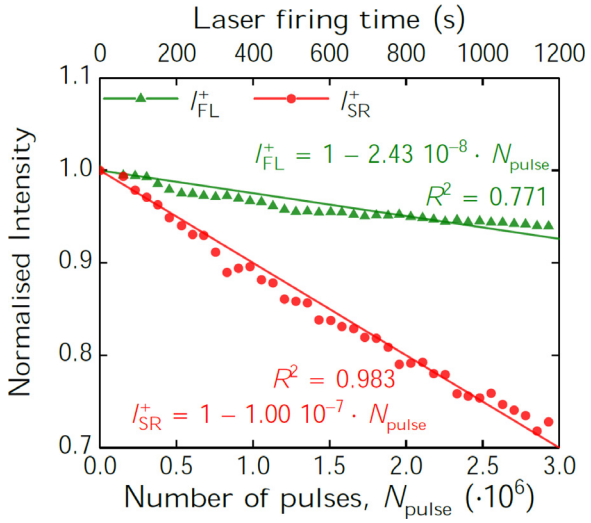

Fig. 14. Photodegradation for both FL and SR at 20 °C induced by the laser light.

over time. Fig. 13 presents the normalized fluorescence intensity of SR over time measured at a water bath of 98°C and at the same concentration as the experiment (i.e., $C_{SR} = 0.15$ kg/m^3). We chose the upper temperature limit below the saturation temperature of water to avoid boiling. We ensured that the volume of the liquid during the runs remained quasi-constant so that any evaporation effects, that would result in an increase of C_{SR}, could be neglected.

For comparison purposes, we also show in Fig. 13 the measurements obtained by Chaze et al. [16] for a similar concentration (i.e., $C_{SR} = 0.15$ kg/m^3) at lower temperatures, spanning a range between 60°C and 80°C. The fluorescence intensity appears to be decreasing in a linear manner for all the temperatures shown. Higher temperatures induce faster degradation of the dye, resulting in smaller slope values. The equation (linear fit) obtained for the 98°C thermal degradation measurements is used to correct the fluorescence intensity values of $I_{f,SR}$ (Fig. 5), since the dye was subjected to varying thermal degradation levels throughout all the experiments performed (boiling and calibration runs).

Appendix B.2. Photo-degradation effects

We subjected a solution of water containing the dyes at the same concentration as the experiments (i.e., $C_{SR} = 0.15$ kg/m^3 and $C_{FL} = 2.695$ kg/m^3) to a laser light of the same frequency and power as the experiments (i.e., 2.5 kHz and 25 W) to investigate the effects of the photo-degradation on the dyes. We recorded the fluorescence emitted over time (and number of pulses) from both dyes. The results are illustrated in Fig. 14. A quasi-linear drop in the fluorescence intensity with time (or the number of pulses) is recorded. We fitted a linear curve with a negative slope, as presented in Fig. 14. The overall firing time of the laser was kept below 100 s throughout the boiling experiments and calibration procedure, so any photo-degradation effects do not need to be accounted for.

Appendix B.3. Dye effects on bubble nucleation and contact angle

We investigated the effects of the added dyes and particles to the water on the nucleation characteristics during pool boiling, by quantifying their effects on: (i) the equivalent diameter of the bubbles during their departure from the heater, and (ii) the nucleation time from their generation to departure. Both quantities are estimated based on shadowgraphy images. The results are illustrated in Table 1 for $q'' = 30$ kW/m^2. The results are averaged over at least five bubbles for each case and the uncertainty of these measurements is taken as one standard deviation.

Table 1
Effect of additives on the bubble nucleation characteristics for $q'' = 30$ kW/m^2.

Additives	Bubble equivalent diameter (mm)	Bubble growth time (ms)
None	2.32 ± 0.16	13.54 ± 2.90
FL	2.38 ± 0.17	14.19 ± 2.79
FL + SR	2.62 ± 0.16	17.12 ± 6.74
FL + SR + Particles	2.44 ± 0.18	14.01 ± 4.33

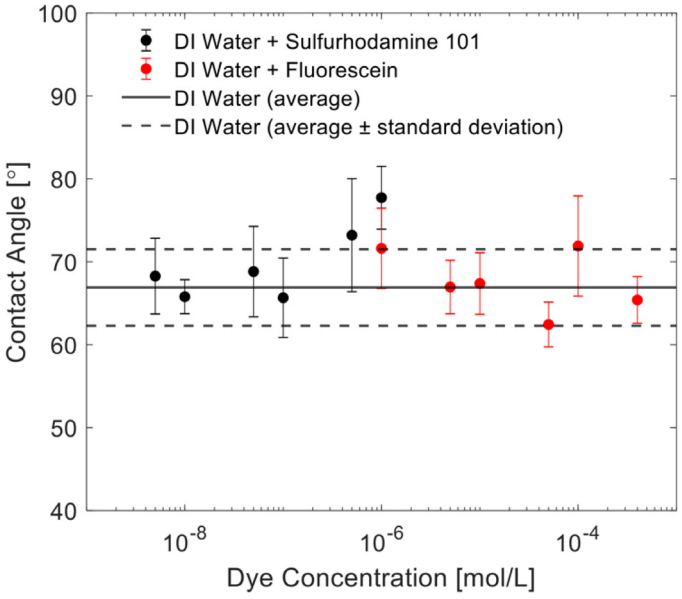

Fig. 15. Effect of dye concentration on the droplet static contact angle.

The addition of the fluorescent dyes, namely FL and SR at their respective concentrations, imposes small changes in the equivalent bubble diameter during departure compared to the additive-free case. These changes are < 13% and within one standard deviation. Similar results were obtained for the nucleation times. We recorded deviations of less than 5%, 26% (exhibiting the greatest standard deviation) and 3% from the additive-free solution, respectively. Notably, all deviations fall within one standard deviation. It is thus confirmed that the additives at the concentrations used do not meaningfully alter the nucleate boiling characteristics at our conditions.

Additionally, droplet static contact angle measurements were performed to verify if the presence of the dyes significantly affects the surface tension. The measurements were done at an ambient temperature of around 20 °C and the droplet volume was kept constant at 4 μL. Six dye concentrations spanning a range of one order of magnitude above and below the concentrations used in the experiments were tested. For each dye concentration, 6 measurements of the contact angle were averaged, and the respective standard deviation is shown in the plot as an error bar. The pure DI water contact angle was determined based on 8 measurements and the average value and standard deviation are shown as continuous and dashed horizontal lines, respectively. These results are shown in Fig. 15.

Most of the contact angle differences between DI water and DI water + dyes solution is within the inherent spreading of the experimental data, which is approximately ± 5° The only exception is for sulfurhodamine 101 around 10^{-6} M, where a small increase is observed. In our experiments, the concentration of sulfurhodamine 101 and fluorescein are kept around 10^{-7} M and 10^{-5} M, respec-

tively. Thus, the fluorescent dyes do not significantly modify the deionized water surface tension.

References

[1] A. Urbano, S. Tanguy, G. Huber, C. Colin, Direct numerical simulation of nucleate boiling in micro-layer regime, Int. J. Heat Mass Transf. 123 (2018) 1128–1137, doi:10.1016/j.ijheatmasstransfer.2018.02.104.

[2] Y. Sato, B. Niceno, Pool boiling simulation using an interface tracking method: from nucleate boiling to film boiling regime through critical heat flux, Int. J. Heat Mass Transf. 125 (2018) 876–890, doi:10.1016/j.ijheatmasstransfer.2018.04.131.

[3] N. Kurul, M.Z. Podowski, Multidimensional effects in forced convection subcooled boiling, International Heat Transfer Conference Digital Library, 1990.

[4] D.B.R. Kenning, V.H. Del Valle M, Fully-developed nucleate boiling: overlap of areas of influence and interference between bubble sites, Int. J. Heat Mass Transf. 24 (6) (1981) 1025–1032, doi:10.1016/0017-9310(81)90133-2.

[5] N. Basu, G.R. Warrier, V.K. Dhir, Wall heat flux partitioning during subcooled flow boiling: Part II - Model validation, J. Heat Transfer 127 (2) (2005) 141–148, doi:10.1115/1.1842785.

[6] S.C.P. Cheung, S. Vahaji, G.H. Yeoh, J.Y. Tu, Modeling subcooled flow boiling in vertical channels at low pressures - Part 1: Assessment of empirical correlations, Int. J. Heat Mass Transf. 75 (2014) 736–753, doi:10.1016/j.ijheatmasstransfer.2014.03.016.

[7] L. Gilman, E. Baglietto, A self-consistent, physics-based boiling heat transfer modeling framework for use in computational fluid dynamics, Int. J. Multiph. Flow 95 (2017) 35–53, doi:10.1016/j.ijmultiphaseflow.2017.04.018.

[8] G.Y. Su, M. Bucci, T. McKrell, J. Buongiorno, Transient boiling of water under exponentially escalating heat inputs. Part I: Pool boiling, Int. J. Heat Mass Transf. 96 (2016) 667–684, doi:10.1016/j.ijheatmasstransfer.2016.01.032.

[9] A. Richenderfer, et al., Investigation of subcooled flow boiling and CHF using high-resolution diagnostics, Exp. Therm. Fluid Sci. 99 (January) (2018) 35–58, doi:10.1016/j.expthermflusci.2018.07.017.

[10] S. Narayan, A. Srivastava, S. Singh, Rainbow schlieren-based investigation of heat transfer mechanisms during isolated nucleate pool boiling phenomenon: effect of superheat levels, Int. J. Heat Mass Transf. 120 (2018) 127–143, doi:10.1016/j.ijheatmasstransfer.2017.12.005.

[11] T. Yabuki, T. Hamaguchi, O. Nakabeppu, Interferometric measurement of the liquid-phase temperature field around an isolated boiling bubble, J. Therm. Sci. Technol. 7 (3) (2012) 463–474, doi:10.1299/jtst.7.463.

[12] M. Takeyama, T. Kunugi, Flow behavior around single nucleate boiling bubble quantitatively grasped by particle tracking visualization, Int. J. Multiph. Flow 129 (2020), doi:10.1016/j.ijmultiphaseflow.2020.103295.

[13] M. Takeyama, M. Zupančič, T. Kunugi, Influence of hydrodynamic interactions among multiple bubbles on convective heat transfer in nucleate boiling, Exp. Therm. Fluid Sci. 128 (April) (2021) 110449, doi:10.1016/j.expthermflusci.2021.110449.

[14] D.A. Walker, A fluorescence technique for measurement of concentration in mixing liquids, J. Phys. E. 20 (2) (1987) 217–224, doi:10.1088/0022-3735/20/2/019.

[15] W. Chaze, O. Caballina, G. Castanet, F. Lemoine, The saturation of the fluorescence and its consequences for laser-induced fluorescence thermometry in liquid flows, Exp. Fluids 57 (4) (2016) 1–18, doi:10.1007/s00348-016-2142-8.

[16] W. Chaze, O. Caballina, G. Castanet, F. Lemoine, Spatially and temporally resolved measurements of the temperature inside droplets impinging on a hot solid surface, Exp. Fluids 58 (8) (2017) 1–16, doi:10.1007/s00348-017-2375-1.

[17] B.L. Smith, D.R. Neal, Particle image velocimetry, Handb. Fluid Dyn., 2nd Ed., 2016 48.1-48.27.

[18] G.M. Aguiar, V. Voulgaropoulos, O.K. Matar, C.N. Markides, M. Bucci, Experimental investigation of bubble nucleation, growth and departure using synchronized IR thermometry, two-colour LIF and PIV, in: 18th International Topical Meeting on Nuclear Reactor Thermal Hydraulics, NURETH, 2019, p. 2019.

[19] M. Bucci, A. Richenderfer, G.Y. Su, T. McKrell, J. Buongiorno, A mechanistic IR calibration technique for boiling heat transfer investigations, Int. J. Multiph. Flow 83 (2016) 115–127, doi:10.1016/j.ijmultiphaseflow.2016.03.007.

[20] J. Sakakibara, R.J. Adrian, Whole field measurement of temperature in water using two-color laser induced fluorescence, Exp. Fluids 26 (1–2) (1999) 7–15, doi:10.1007/s003480050260.

[21] M.B. Shafii, C.L. Lum, M.M. Koochesfahani, In situ LIF temperature measurements in aqueous ammonium chloride solution during uni-directional solidification, Exp. Fluids 48 (4) (2010) 651–662, doi:10.1007/s00348-009-0758-7.

[22] A. Sciacchitano, et al., Collaborative framework for PIV uncertainty quantification: comparative assessment of methods, Meas. Sci. Technol. 26 (7) (2015), doi:10.1088/0957-0233/26/7/074004.

[23] B... Mikic, W... Rohsenow, P. Griffith, On bubble growth rates, Int. J. Heat Mass Transf. 13 (4) (1970) 657–666, doi:10.1016/0017-9310(70)90040-2.

[24] K. Schweikert, A. Sielaff, P. Stephan, On the transition between contact line evaporation and microlayer evaporation during the dewetting of a superheated wall, Int. J. Therm. Sci. 145 (June) (2019) 106025, doi:10.1016/j.ijthermalsci.2019.106025.

[25] C. Kunkelmann, K. Ibrahem, N. Schweizer, S. Herbert, P. Stephan, T. Gambaryan-Roisman, The effect of three-phase contact line speed on local evaporative heat transfer: experimental and numerical investigations, Int. J. Heat Mass Transf. 55 (7–8) (2012) 1896–1904, doi:10.1016/j.ijheatmasstransfer.2011.11.044.

[26] K. Cole, J. Beck, A. Haji-Sheikh, B. Litkouhi, Heat Conduction Using Greens functions, Taylor & Francis, 2010.

[27] T. Tanaka, K. Miyazaki, T. Yabuki, Observation of heat transfer mechanisms in saturated pool boiling of water by high-speed infrared thermometry, Int. J. Heat Mass Transf. 170 (2021) 121006, doi:10.1016/j.ijheatmasstransfer.2021.121006.

[28] A. Kossolapov, B. Phillips, M. Bucci, Can LED lights replace lasers for detailed investigations of boiling phenomena? Int. J. Multiph. Flow 135 (2021) 103522, doi:10.1016/j.ijmultiphaseflow.2020.103522.